

**Journal of Geophysical Research: Solid Earth****RESEARCH ARTICLE**

10.1002/2015JB012505

**Key Points:**

- The temporal evolution of ground deformation associated with the 2009 Harrat Lunayyir intrusion is observed by InSAR
- Stress calculations provide insights into the interplay between dike intrusion and faulting
- Analog experiments suggest that the width of the wedge-shaped graben corresponds to the depth of the dike

**Correspondence to:**

W. Xu,  
wenbin.xu@kaust.edu.sa

**Citation:**

Xu, W., S. Jónsson, F. Corbi, and E. Rivalta (2016), Graben formation and dike arrest during the 2009 Harrat Lunayyir dike intrusion in Saudi Arabia: Insights from InSAR, stress calculations and analog experiments, *J. Geophys. Res. Solid Earth*, 121, doi:10.1002/2015JB012505.

Received 24 SEP 2015

Accepted 28 FEB 2016

Accepted article online 4 MAR 2016

## Graben formation and dike arrest during the 2009 Harrat Lunayyir dike intrusion in Saudi Arabia: Insights from InSAR, stress calculations and analog experiments

Wenbin Xu<sup>1,2</sup>, Sigurjón Jónsson<sup>1</sup>, Fabio Corbi<sup>3,4</sup>, and Eleonora Rivalta<sup>3</sup>

<sup>1</sup>Physical Science and Engineering Division, King Abdullah University of Science and Technology, Thuwal, Saudi Arabia,

<sup>2</sup>Now at Department of Earth and Planetary Sciences, University of California, Berkeley, California, USA, <sup>3</sup>GFZ German Research Centre for Geosciences, Potsdam, Germany, <sup>4</sup>Dipartimento di Scienze, Roma Tre University, Rome, Italy

**Abstract** Detailed spatial and temporal accounts of propagating dikes from crustal deformation data, including their interplay with faulting, are rare, leaving many questions about how this interplay affects graben formation and the arrest of dikes unanswered. Here we use interferometric synthetic aperture radar (InSAR) observations, stress calculations, and analog experiments to investigate the interaction between an intruding dike and normal faulting during the 2009 Harrat Lunayyir dike intrusion in western Saudi Arabia. We generated five displacement maps from InSAR data to unravel the temporal evolution of deformation covering the majority of the intrusion. We find that the observed surface displacements can be modeled by a ~2 m thick dike with an upper tip ~2 km below the surface on 16 May 2009, 4 weeks after the onset of seismic unrest. In the following three days, the dike propagated to within ~1 km of the surface with graben-bounding normal faulting dominating the near-field deformation. The volume of the dike doubled between mid-May and mid-June. We carried out analog experiments that indicate that the wedge-shaped graben grew outward with the faulting style changing progressively from normal faulting to oblique. Coulomb failure stress change calculations show that the intruding dike caused two zones of shallow horizontal tension on both sides of the dike, producing two zones of fissuring and normal faulting at the surface. In return, the faulting provoked compression around the upper tip of the dike, holding back its vertical propagation.

### 1. Introduction

Dike intrusions induce stress changes in the surrounding rock, leading to seismicity and deformation as well as movement on faults [Rubin and Pollard, 1988]. The interplay between magma emplacement and fault activation is integral to volcano tectonics because it controls the formation and evolution of topography in rift zones [Buck *et al.*, 2006]. Furthermore, this interplay affects volcanic and seismic hazards, as large earthquakes are sometimes triggered or entirely induced by dikes [Passarelli *et al.*, 2012]. Moreover, faulting can alter the dynamics of diking toward increasing the likelihood of an eruption [Rivalta and Dahm, 2004; Le Corvec *et al.*, 2013] or arrest the dike [Maccaferri *et al.*, 2016].

At least three key case studies from the East African Rift and Iceland have provided relevant insights about the link between dike intrusions and fault activation. The Manda Hararo-Dabbahu rifting episode commenced in September 2005 with a massive dike intrusion that was ~4 m thick on average over its 60–70 km length [Wright *et al.*, 2006; Rowland *et al.*, 2007]. The dike did not reach the surface along most of its length but caused extensive graben-bounding normal faulting with the flanks uplifting by up to 2 m and the graben floor subsiding by up to 3 m [Ebinger *et al.*, 2010]. The initial dike was followed by 13 smaller dike injections during the 5 year long rifting episode [Wright *et al.*, 2012], each showing deformation due to concurrent magma intrusions and faulting [Grandin *et al.*, 2009; Hamling *et al.*, 2009]. Calculations of stress changes between consecutive dike injections indicate that the subsequent dike was preferentially emplaced where tensile stresses had been increased by the preceding dike intrusion [Grandin *et al.*, 2010; Hamling *et al.*, 2010]. However, analysis of interactions between diking and faulting was prevented by severe decorrelation of interferometric synthetic aperture radar (InSAR) data in the graben, where the most intense deformation occurred [Grandin *et al.*, 2010].

In northern Tanzania, InSAR observations of a rifting event in 2007 provided rich measurements of the ground deformation, allowing the pattern of diking and faulting in the upper crust to be determined [Baer et al., 2008]. Inverse modeling of the temporal series of surface deformation data suggests that normal faulting dominated the first week of the event, but that dike opening and dike-induced shallow graben-bounding faulting dominated the following months [Baer et al., 2008; Biggs et al., 2009; Biggs et al., 2013; Calais et al., 2008]. Based on calculations of stress changes, the authors suggested that a deep dike (not detected by geodetic observations) caused sufficient static stress changes to trigger movement on the blind normal fault [Biggs et al., 2013; Calais et al., 2008]. Activation of this fault reduced normal stress in its vicinity, facilitating the continued upward propagation of the dike to shallower levels within the crust, which eventually triggered normal slip on shallow graben-bounding faults [Baer et al., 2008; Biggs et al., 2009; Biggs et al., 2013; Calais et al., 2008].

The recent Bárðarbunga rifting event of 2014–2015 was associated with a lateral dike intrusion away from the subglacial Bárðarbunga caldera. This dike intrusion caused widespread deformation with surface displacements exceeding 30 cm at several GPS sites [Sigmundsson et al., 2015]. In the near field, a series of high-resolution radar amplitude image offsets show a narrow graben structure at the surface bounded by two subparallel border faults with several meters of fault displacement on each (J. Ruch et al., Oblique rift opening revealed by recurrent magma injection in central Iceland, *Nature Communications*, in revision, 2016). The graben formed above the propagating dike during the rifting event, and the dike erupted where the two subparallel normal faults converged toward each other (J. Ruch et al., in revision, 2016).

The temporal resolution of InSAR data is rarely sufficient to appreciate the rapid evolution of dike intrusions. Geodetic observations of recent rifting events in the East African Rift and in Iceland have thus only offered a picture of the cumulative ground deformation of the entire dike-intrusion process. From an imaging point of view, the dynamics of the dike-fault interaction is largely unexplored. Instead, field studies, numerical models, and analog experiments have been used to understand the kinematics and dynamics of diking and the causal relationship between shallow dike intrusions and extensional fracturing and faulting of the surface [Mastin and Pollard, 1988; Tripanera et al., 2014]. Mastin and Pollard [1988] performed analog experiments to study the surface effects of dike inflation and found that shallow dike emplacements generate a syncline between two gentle topographic highs on each side above the dike. These topographic highs become zones of extensional strain. As the dike continues to inflate, fissures progressively propagate downward from the surface toward the tip of the dike. During the final stage, a graben develops above the dike due to dip-slip movement on some of the extensional fractures. Using a frictional-law criterion, Rubin and Pollard [1988] further demonstrated that dike intrusions always trigger surface faulting and not vice versa; however, their explanation focused on inferred fault behavior as a consequence of the dike intrusion and did not consider the impact of normal faulting on the intruding dike. Maccaferri et al. [2016] developed a numerical model for the interaction of the 2000 intrusion at Miyakejima with a preexisting active strike-slip fault system hit by the dike tip during propagation. They found that the interaction with the fault was the main cause of the dike's arrest provided the fault was tectonically preloaded. They concluded that a dike will unlikely get arrested just as a result of faulting induced by its propagation, but their model setup did not consider interaction with the free surface or graben faulting.

Here we focus on analyzing spatial and temporal variability of deformation during the 2009 Harrat Lunayyir dike intrusion, enabled by favorable acquisition programming of the Envisat satellite. We first review the earthquake activity associated with the intrusion crisis and then present five InSAR surface displacement maps that illustrate the growing deformation. From these, we estimated source parameters for the faulting and the dike. Finally, we focus on the interplay between the dike and the faults by analyzing Coulomb failure stress change calculations and results of analog experiments, which together provide information about the dynamics of the dike (deceleration and arrest) and the graben formation.

## 2. Overview of the 2009 Harrat Lunayyir Crisis

Harrat Lunayyir is one of the smallest and youngest of the extensive volcanic fields on the western Arabian Peninsula, lying ~60 km east of the Red Sea and covering a surface area of ~3500 km<sup>2</sup> (Figure 1) [Roobol, 2009]. Historical records of volcanic activity indicate that over 20 eruptions have occurred on the Arabian Peninsula during the past 2000 years [Camp et al., 1987], including one possible eruption in Harrat Lunayyir about 1000 years ago.

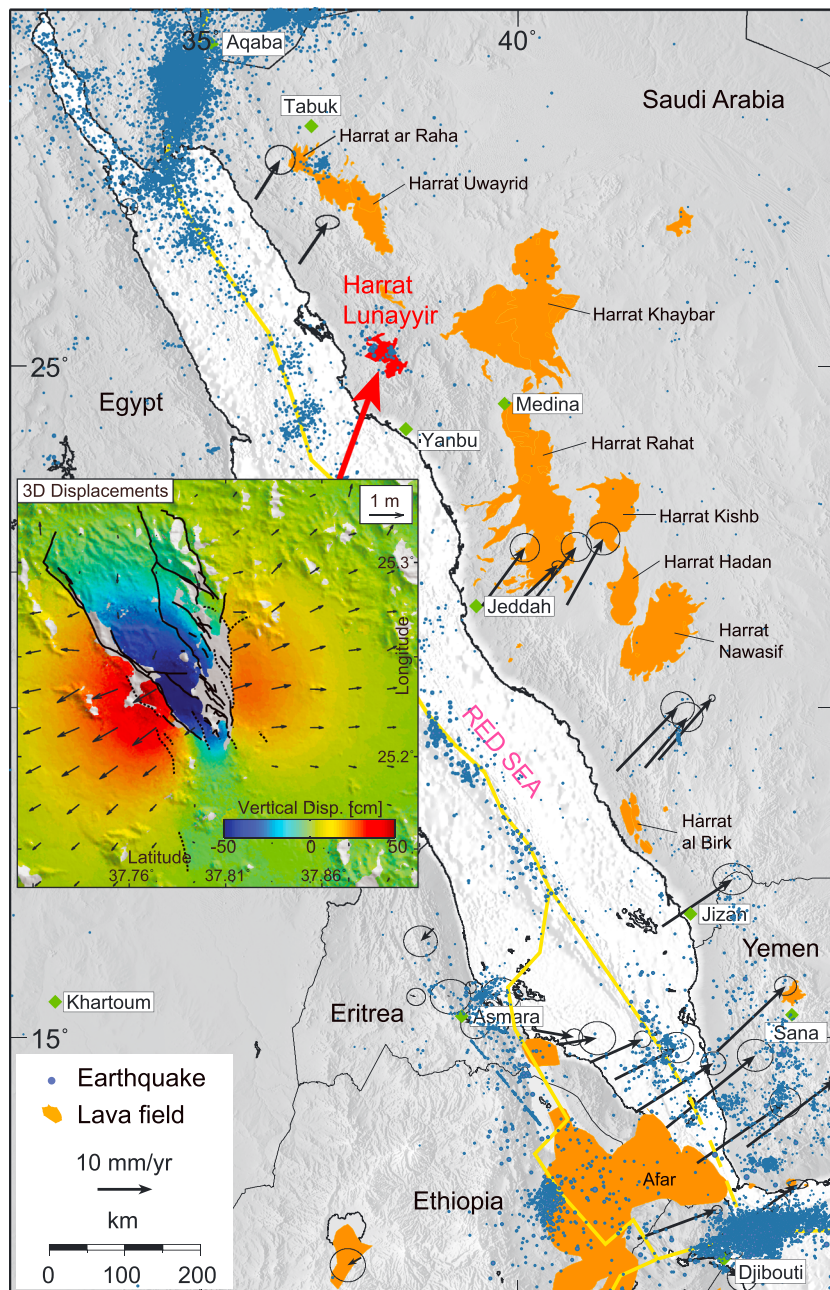


**Figure 1.** Map of the Red Sea showing the locations of Harrat Lunayyir (red) and other Harrat lava fields (orange). Blue dots show two decades of seismicity from the ISC catalog, yellow lines mark plate boundaries, and black arrows show GPS velocities with 95% confidence ellipses in a Eurasia-fixed reference frame [ArRajehi *et al.* 2010]. The inset shows derived 3-D surface displacements of the 2009 activity in Harrat Lunayyir (with the background color map showing vertical and horizontal displacements) with mapped faults and fractures shown as black lines [from Jónsson, 2012].

The first sign of new activity in Harrat Lunayyir was in October 2007, when an earthquake swarm started with about 500 recorded events and lasted until May 2008. The maximum earthquake magnitude ( $M$ ) of the sequence was 3.2 with event locations showing a NE-SW trend, suggested to have occurred below 10 km (Figure 2). Later, between April and July 2009, a much stronger seismic swarm of more than 30000 recorded earthquakes struck the area with many events of  $M > 4$ , located about 15 km northwest of the 2007 swarm (Figure 2). The threat of more large earthquakes and a possible eruption prompted the authorities to evacuate about 40,000 people from the region. An expeditious effort was made to collect scientific data of this rare activity on the Arabian

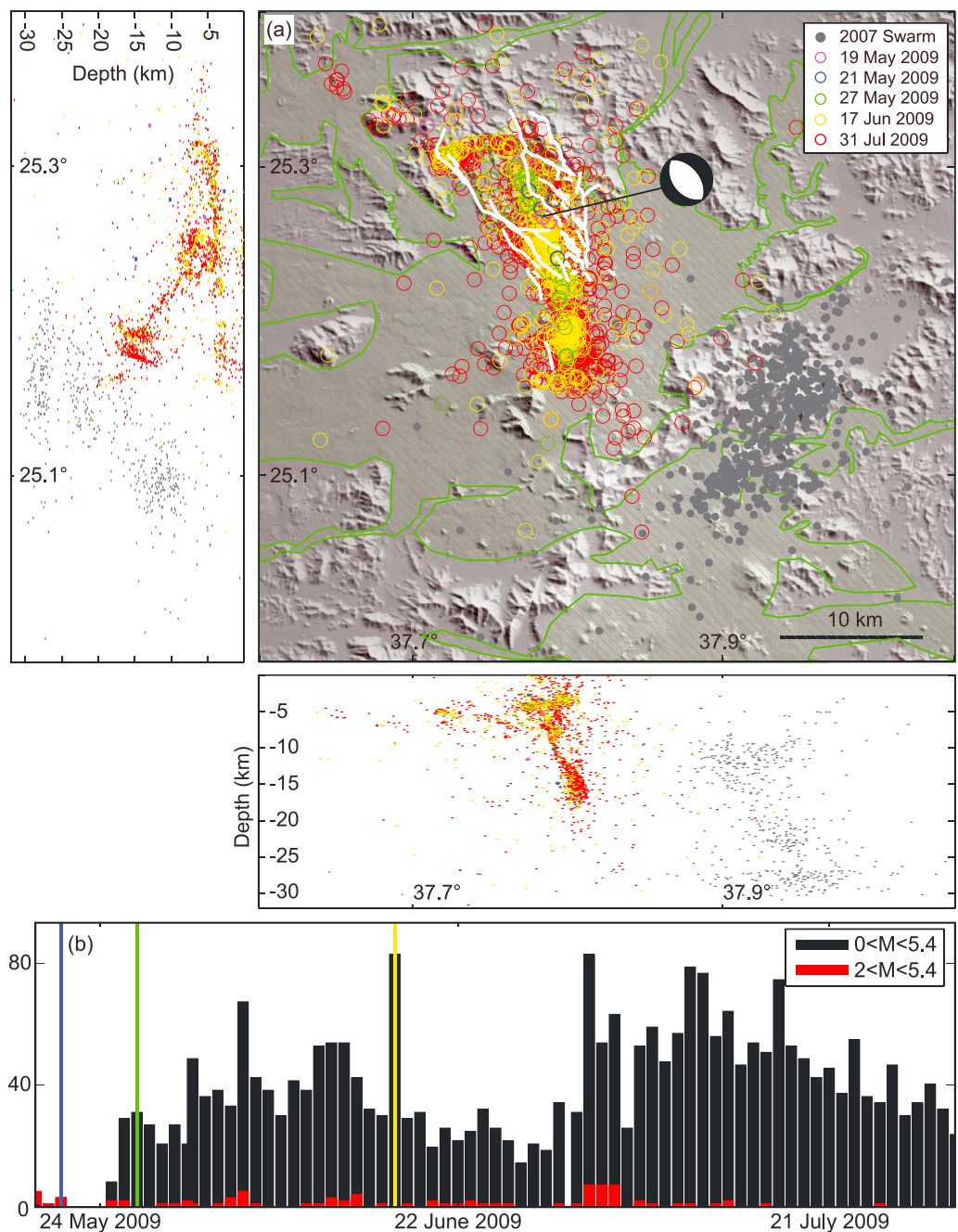


**Figure 2.** Earthquakes recorded during the 2009 activity at Harrat Lunayyir [from Hansen et al., 2013]. (a) White lines mark mapped faults and fractures from Jónsson [2012] and green lines mark edges of lava flows. The focal mechanism of the  $M_w 5.7$  19 May 2009 main shock is also shown. (b) Temporal variations in daily number of earthquakes ( $M > 0$ , black;  $M > 2$ , red) recorded in Harrat Lunayyir. Vertical colored lines correspond to the dates in Figure 2a.

Peninsula [Pallister et al., 2010]. Field observations and InSAR data show that the earthquake swarm was accompanied by surface fracturing and faulting of up to ~14 km in length with vertical offsets of ~1 m. Results from both the data that were collected and from modeling and interpretation indicate that the activity was caused by a dike intrusion that ascended to ~1 km below the surface, nearly initiating a volcanic eruption [Pallister et al., 2010; Jónsson, 2012].

Most  $M > 4$  earthquakes occurred before 21 May 2009 with the largest earthquake of moment magnitude 5.7 taking place on 19 May (the main event). The mechanisms of the  $M > 4$  events were predominantly normal

faulting with a minor strike-slip component [Hansen *et al.*, 2013; Pallister *et al.*, 2010], consistent with the regional stress field and the 3-D stresses induced by a subvertical dike [Passarelli *et al.*, 2015]. Hansen *et al.* [2013] relocated ~5700 earthquakes that occurred between 30 April and 31 July 2009, although most occurred after 19 May when the seismic network had been improved. The estimated accuracy of these relocated events is 0.36 km laterally and 0.63 km in depth [Hansen *et al.*, 2013]. Most earthquakes cluster between depths of 5 km and 15 km (Figure 2a). Unlike the swarm in 2007–2008, the 2009 swarm was mainly orientated in the NNW-SSE direction on a steeply dipping plane (Figure 2a). Assuming that the earlier swarm was caused by the dike propagation during its first stage of ascent, the seismicity as a whole indicates an inclined pathway of magma under Harrat Lunayyir. However, insufficient data were collected to determine the initial location and geometry of this pathway.

Along with the earthquake relocations, Hansen *et al.* [2013] also generated a *P* wave velocity model beneath Harrat Lunayyir using local double-difference tomography. They found a high velocity anomaly at ~15 km below the surface with a similar orientation as the 2009 seismic swarm. The group interpreted this as a zone of repeated dike intrusions and suggested that future seismic and volcanic hazards are possible in the region. Koulakov *et al.* [2014] obtained a 3-D seismic attenuation model of the crust beneath Harrat Lunayyir and found low-attenuation zones above 5 km depth and high-attenuation zones below 6 km depth. This group interpreted the high-attenuation zones as corresponding to the upper part of the magma conduit and the low-attenuation zones as corresponding to rigid rocks. More recently, the same group presented a new tomographic model of *P* and *S* velocities and suggested that a magma reservoir is likely located at 7 km with a conduit below it [Koulakov *et al.*, 2015]. However, these results are in contrast to the findings of Duncan and Al-Amri [2013], who dated and analyzed six volcano stratigraphic units in Harrat Lunayyir to find evidence of lithospheric thinning and indicators that the erupted magmas came from the upper mantle without significant residence time in the crust.

Multiple ascending and descending InSAR observations from the Envisat and ALOS satellites and multiple aperture interferometric along-track measurements were used to invert the 3-D ground displacement field caused by the intrusion [Baer and Hamiel, 2010; Jónsson, 2012]. These 3-D maps clearly show ~1.5 m of extension in the east-west direction, over 60 cm of vertical offset on the western graben-bounding normal fault, and 10–20 cm tensional fractures on the eastern side (Figure 1). The surface deformation associated with the dike intrusion is best modeled by a ~10 km long near-vertical opening with a ~340° strike and two NNW-SSE oriented normal faults forming a wedge-shaped graben [Baer and Hamiel, 2010; Pallister *et al.*, 2010]. Based on this information and on derived 3-D surface displacements from InSAR data, Jónsson [2012] estimated the tensile strength of the granitic rock mass (under the basalts) as 1–3 MPa.

### 3. InSAR Observations of Dike Propagation and Faulting

#### 3.1. InSAR Data Processing

To investigate the temporal evolution of the dike intrusion and faulting, we used radar data from the Envisat satellite (C band, 5.6 cm wavelength) acquired in image and wide swath modes from both ascending and descending orbits (Table 1). Wide swath data have an average spatial resolution of ~150 m in the range (across track) direction, while those in the image mode have a higher resolution of ~20 m. We processed five interferograms that spanned the height of the activity of the intrusion, separated by only a few days and produced a series of ground deformation maps. We processed the data with the GAMMA software and used the Shuttle Radar Topography Mission (SRTM) 3 arc second digital elevation model (DEM) [Farr *et al.*, 2007] to simulate and eliminate topographic signals. Noise in the interferograms was first reduced by multilooking to about 80 m pixel spacing and then by filtering [Goldstein and Werner, 1998]. The interferograms were unwrapped using the minimum cost flow method [Chen and Zebker, 2000] and finally geocoded into the WGS84 coordinate system.

To mitigate residual orbital and long wavelength atmospheric errors, we first masked the deforming area out and fitted a quadratic plane to the remaining data in the surrounding nondeforming areas. We then subtracted the estimated surface from the interferograms to obtain deformation interferograms. We also reduced elevation-dependent atmospheric signals in the interferograms, by estimating and removing a linear trend between elevation and unwrapped InSAR phases. After these operations, residual orbital errors

**Table 1.** Envisat SAR Data Used in This Study<sup>a</sup>

Mode	Flight Direction	Incidence Angle	Start Date	End Date	Perp. B (m)
Wide swath	Ascending	29°	21 July 2007	16 May	3
Wide swath	Ascending	38°	14 April	19 May	192
Wide swath	Descending	38°	1 January	21 May	-100
Image mode	Descending	23°	14 January 2004	27 May	-91
Image mode	Ascending	23°	28 July 2004	17 June	32

<sup>a</sup>All dates are from 2009 unless otherwise stated.

and atmospheric signals are considerably reduced in the interferograms in the area of interest around the dike intrusion.

### 3.2. Inversion for Dike Opening and Fault Slip

To model the intrusion of the dike and movement on the faults we used rectangular dislocations in a homogeneous, isotropic, elastic half space [Okada, 1985] with Poisson's ratio and shear modulus of 0.25 and 25 GPa, respectively. We used data acquired prior to 16 May 2009 to estimate the dike geometry using a Monte-Carlo-type simulated annealing algorithm [Cervelli *et al.*, 2001]. We found the dike to be dipping 87° toward the southwest and oriented N343°E, which is similar to the dike geometry estimated by Pallister *et al.* [2010], who found a dip of 89° toward the southwest and oriented N343°E. We then used the estimated dike geometry and applied least squares inversion to determine the amount of dike opening and fault slip on the graben-bounding faults that fit best with the InSAR data set. The InSAR data were subsampled using the quadtree method and weighted using the inverse of their variance [Jónsson *et al.*, 2002]. To account for the spatially variable dike opening and fault slip distribution we subdivided the dislocation planes into 1 km × 1 km patches. For data acquired after 16 May, we included both dike opening and fault slip in the modeling. To prevent oscillatory solutions, the inversion was regularized with positivity and smoothness constraints [Jónsson *et al.*, 2002] and the dike volume was made to steadily increase with time. The uncertainty of the volume change was estimated using the so-called randomize-then-optimize method [Bardsley *et al.*, 2014]. In this method, we modified the original data by adding random noise and generated multiple data realizations (here 100 realizations). From each of these data realizations, we estimated the volume change; the distribution of the estimated volume change values reflects the uncertainty in volume change.

### 3.3. Observed Deformation and Modeling Results

The first sign of deformation associated with the Harrat Lunayyir activity was seen in the Envisat interferogram covering the first 4 weeks of the swarm (up to 16 May 2009). Although one Envisat image was acquired earlier during the swarm (8 May, data not shown), it did not show any obvious ground deformation. This indicates that the Harrat Lunayyir earthquake activity began at least 3 weeks before any detectable deformation occurred at the surface.

#### 3.3.1. Deformation up to 16 May 2009

This interferogram (21 July 2007 to 16 May 2009) shows the ground deformation up to 3 days prior to the main earthquake on 19 May (Figure 3a). The observed elliptically shaped deformation pattern is typical for what might be expected from a buried dike opening. About ~14 cm of line-of-sight (LOS) decrease is apparent on the western side as is a ~7 cm LOS increase at the center of the interferogram. Results from the modeling show that by this stage the dike had ascended to ~2 km below the surface with a maximum opening of ~1.9 m and a volume of  $\sim 0.06^{+0.011}_{-0.008}$  km<sup>3</sup>.

#### 3.3.2. Deformation up to 19 May 2009

This interferogram (14 April 2007 to 19 May 2009) covers three additional days of activity compared to the previous interferogram and includes the main event of the swarm ( $M = 5.7$ ) on 19 May (Figure 3b). The earthquake occurred at 17:35 UTC, while the radar scene was acquired 2 h later at 19:33 UTC. The interferogram shows two lobes of fringes on each side of the graben and a broad area of deformation. The deformation pattern is consistent with what might be expected from a dike with induced surface faulting bounding a graben [e.g., Nobile *et al.*, 2012]. InSAR coherence is lost in the graben, mainly due to the large deformation gradients in this area, which are not resolved in this medium resolution wide-swath data. Around 57 cm and 13 cm of LOS uplift are seen on the western and eastern flanks of the graben in this interferogram, respectively. The elastic model indicates that the dike had ascended to ~1 km below the surface by this date. We estimated

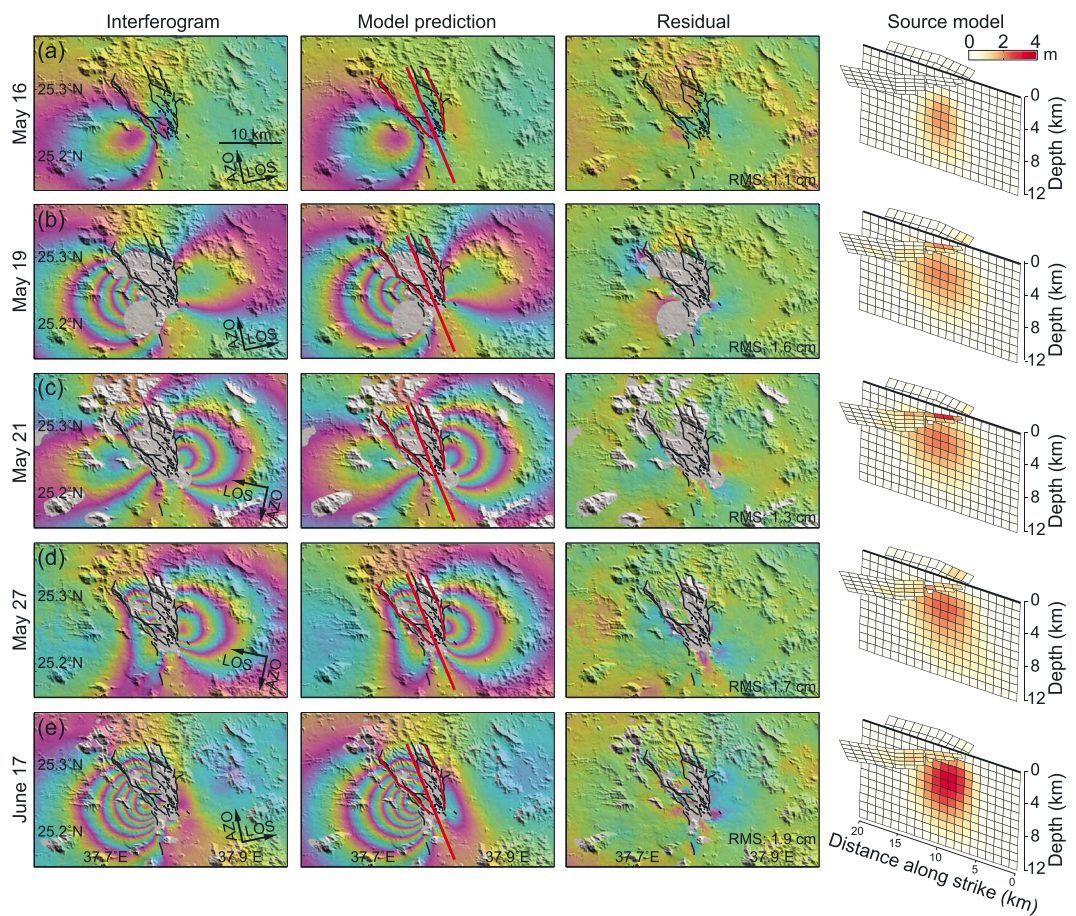


**Figure 3.** (from left to right) Observed (first column) interferograms, (second column) model predictions, (third column) residuals, and (fourth column) model sources for (a–e) time periods covering increasing portions of the 2009 Harrat Lunayyir dike intrusion. The interferograms were unwrapped and then rewrapped with each fringe representing a 10 cm displacement in line-of-sight direction. Note the different line-of-sight directions for the ascending and descending orbit data. Black lines mark mapped faults and fractures, and red lines the model dike (thicker) and graben-bounding normal faults.

up to 2 m of slip on the graben-bounding normal faults, although the slip is not well resolved due to missing observations near the graben. The dike is estimated to have opened to a maximum of ~2 m and increased to a volume of  $\sim 0.1^{+0.012}_{-0.015} \text{ km}^3$ .

### 3.3.3. Deformation Until 21 May 2009

This interferogram (1 January 2009 to 21 May 2009) was acquired from a descending orbit and thus shows more fringes on the eastern side, ~38 cm LOS uplift compared with ~18 cm on the western side of the dike (Figure 3c), than the previous interferograms. Results of the modeling show that the pattern of dike opening was similar to that of the previous interferogram without any additional upward migration, although the estimated volume of the dike increased to  $\sim 0.11^{+0.017}_{-0.005} \text{ km}^3$  during the last 2 days.

### 3.3.4. Deformation up to 27 May 2009

This interferogram (14 January 2004 to 27 May 2009) was obtained in an image mode with a steeper incidence angle than the previous interferograms (Figure 3d). It has better coherence in the graben and is more sensitive to vertical deformation. Three fringes on the eastern side of the dike (30 cm) and a high fringe gradient in the graben (with up to 53 cm LOS displacement) are evident. The elastic model indicates that the maximum dike opening and volume increased to ~2.3 m and  $\sim 0.13^{+0.007}_{-0.009} \text{ km}^3$ , respectively.

### 3.3.5. Deformation up to 17 June 2009

This interferogram (11 October 2006 to 17 June 2009) includes the majority of the deformation associated with the crisis (Figure 3e). Over 1 m of east-west extension in LOS is observed and the modeled dike has opened to 3.3 m. The opening is greatest at 2–7 km below the surface with little opening occurring below

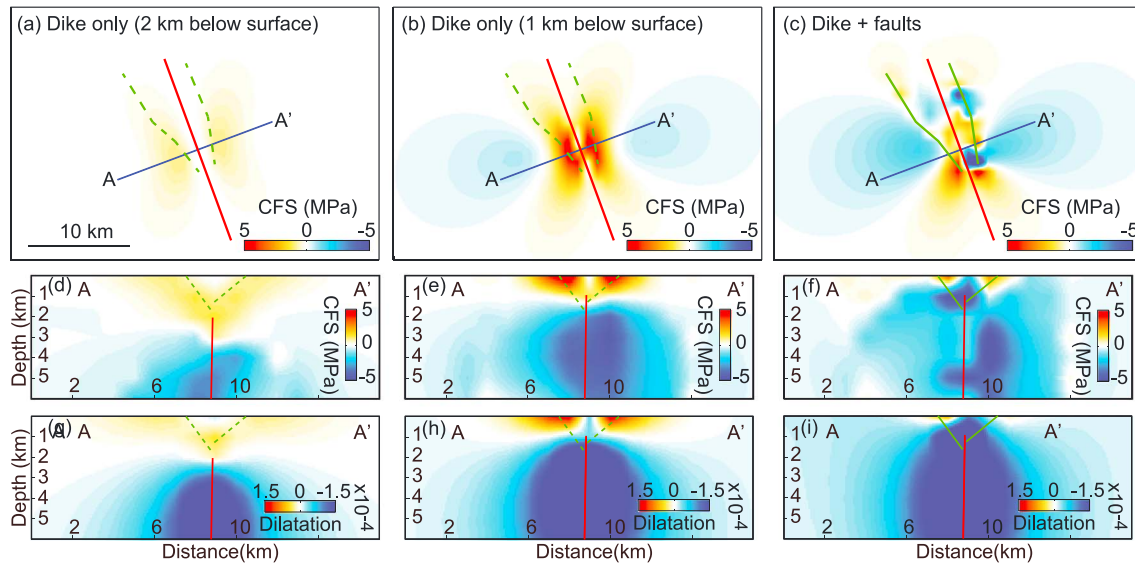


**Figure 4.** Calculated Coulomb failure stress changes ( $\Delta\text{CFS}$ ) resolved on optimally oriented normal faults showing the stress interactions between the dike injection and normal faulting. (a)  $\Delta\text{CFS}$  for a dike-only model 2 km below the surface, (b)  $\Delta\text{CFS}$  for a dike-only model 1 km below the surface and (c)  $\Delta\text{CFS}$  for a dike-fault model. (d–f) Cross-sections A-A' of Figures 4a–4c. (g–i) Cross sections showing dilatational strain.

7 km or above 1 km. Results of the modeling suggest that a total volume of  $\sim 0.14^{+0.006}_{-0.026} \text{ km}^3$  of magma intruded along the 10 km long segment during the 1 month period. Although the seismicity continued after 17 June, only  $\sim 5\%$  additional deformation occurred after this date [Pallister *et al.*, 2010].

#### 4. Stress Calculations

Coulomb failure stress change ( $\Delta\text{CFS}$ ) calculations have been widely used to explore how earthquakes are triggered due to stress changes at volcanoes [Lin and Stein, 2004; Toda *et al.*, 2005]. The Coulomb failure model can be simplified as

$$\Delta\text{CFS} = \Delta\tau + \mu' \Delta\sigma, \quad (1)$$

where  $\Delta\tau$  is the shear stress change on the receiver fault,  $\mu'$  is the effective coefficient of friction, and  $\Delta\sigma$  is the normal stress change. Failure is promoted if  $\Delta\text{CFS}$  is positive and inhibited if it is negative [see, e.g., Freed, 2005].

To model the static stress interactions between the dike injection and normal faulting in Harrat Lunayyir we imported our estimated elastic dislocation models into the Coulomb 3.4 software [Lin and Stein, 2004; Toda *et al.*, 2005] and calculated the  $\Delta\text{CFS}$  using an effective coefficient of friction of 0.4. We calculated the  $\Delta\text{CFS}$  on optimally oriented normal faults for each location at the surface to explore how much dike-induced stress change is needed to trigger faulting. Conversely, we also investigated how the normal fault slip affects the stress around the dike.

##### 4.1. Stress Changes due to a 2 Km Deep Dike

For an ascending dike that is 2 km below the surface (Figure 3a), the calculated  $\Delta\text{CFS}$  show two regions of increased stress of up to 1 MPa on each side of the dike (Figure 4a). In cross section, the two positive  $\Delta\text{CFS}$  zones can clearly be identified above the tip of the dike and inclining toward it (Figure 4d). A large compression perpendicular to the dike causes large negative dilatational strains and negative  $\Delta\text{CFS}$  (Figures 4d and 4g). At this stage, no obvious normal faulting had occurred in Harrat Lunayyir.

##### 4.2. Stress Changes due to a 1 Km Deep Dike

When the growing dike reaches within 1 km below the surface,  $\Delta\text{CFS}$  caused by the dike intrusion acting on the surface increases dramatically to  $\sim 6 \text{ MPa}$  (Figure 4b). Two zones of maximum horizontal tension are clearly visible at the surface on opposite sides of the dike plane (Figures 4e and 4h). These regions favor the initiation of open cracks and produce two zones of fissuring and normal faulting [Mastin and Pollard, 1988]. As the dike

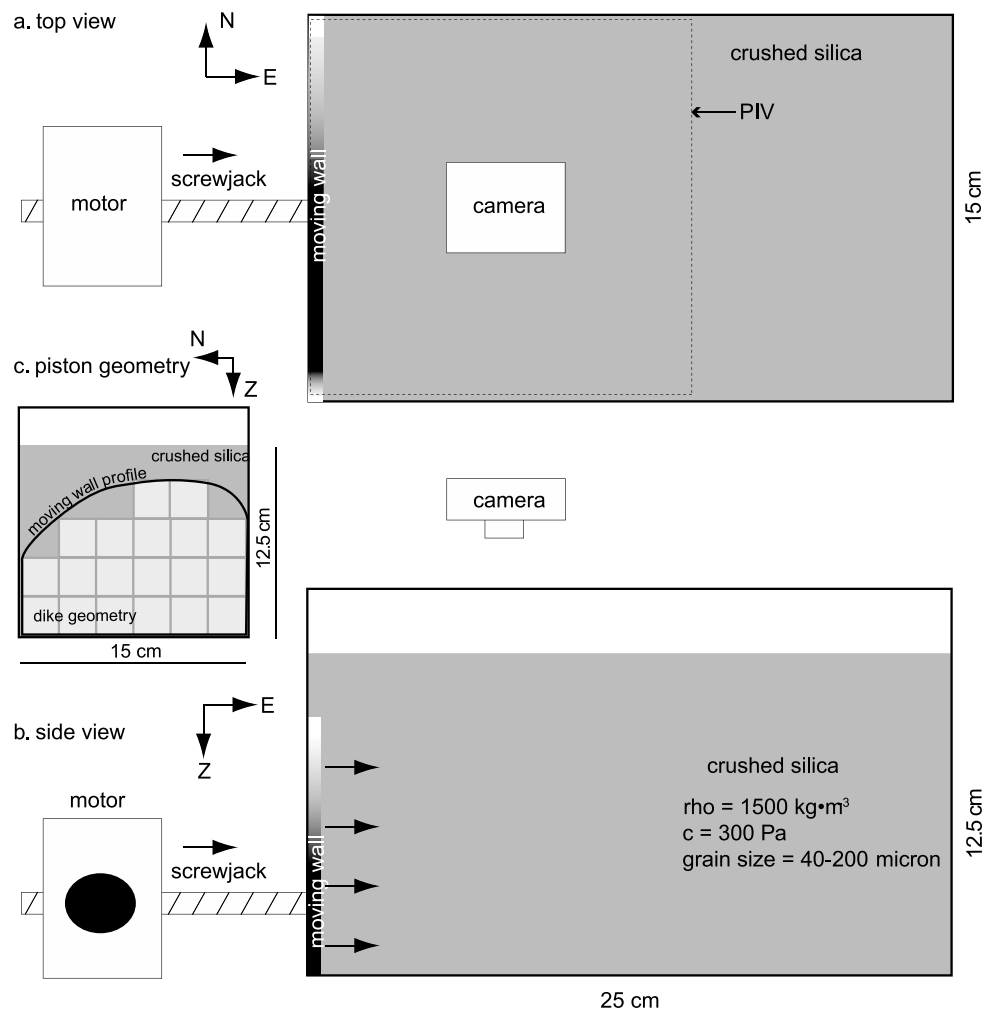


**Figure 5.** Schematic of the analog experimental setup. (a) Top view with the dashed box representing the area that was analyzed by PIV in Figure 6. (b) Side view of the experimental set up. (c) Piston geometry with the black line representing the shape of the moving wall and gray squares referring to the final estimated dike geometry at Harrat Lunayyir on 17 June.

approaches the surface, the distance between the two high-strain zones decreases (Figure 4h). Eventually, this process leads to the formation of graben above the dike.

#### 4.3. Stress Relief by Normal Faulting

Slip on conjugate normal faults above a dike is expected to relieve a large proportion of the tensional stresses at the surface and some of the compressional stresses around the dike (Figures 4c and 4f). If faulting is included in the calculation, the stress change above the tip of the dike changes from extension to compression. In comparison to the dike-only model, the value and area of the  $\Delta\text{CFS}$  at the surface and the dilatational strain decrease significantly (Figure 4i), which indicates that the movement of the graben-bounding faults may have stopped the upward propagation of the dike.

### 5. Analog Experiments

The CFS modeling shows what elastic stress changes can be expected from the dike intrusion and the normal faulting, but it does not provide direct information about the fracture initiation or about how the fractures grow into normal faults. Analog experiments, on the other hand, can offer a picture of the evolving surface deformation through time, including how extensional fractures and faults form at the surface and grow with

increasing dike opening. Therefore, we designed an analog experiment to reproduce some aspects of the observed deformation in Harrat Lunayyir and analyzed the controlling parameters.

### 5.1. Analog Experimental Setup

Our experimental setup consisted of a 15 cm wide and 25 cm long box filled with crushed silica powder, which functioned as a brittle rock analog (Figure 5). This setup scales the physical properties of the upper crust [Norini and Acocella, 2011; Ruch *et al.*, 2012; Tripanera *et al.*, 2014], providing a length scaling factor in the range of  $10^{-4}$ – $10^{-5}$  depending on the cohesion of rocks in nature [Hubbert, 1937], and in our case a length scaling factor of  $2.5 \times 10^{-5}$ : 2.5 cm in the model was equivalent to 1 km in nature. Note that the dike opening is not scaled as the other length dimensions [Tripanera *et al.*, 2014]. The box featured a moving sidewall that is pushed inward by a screw jack controlled by a stepping motor. We shaped the moving wall as an asymmetrical arc where the highest point is at two thirds of the dike length, resembling the final stage of the 2009 Harrat Lunayyir intrusion (Figure 4c).

The experiment uses the dike as a plane of symmetry (i.e., the model reproduces only one side of the host rocks and a vertical dike is assumed). The experimental dike opening is homogeneous on the surface of the dike and increases from 0 to 0.6 cm. This means that only the inflation of a dike having a similar shape as the Harrat Lunayyir intrusion was modeled, but neither the distributed dike opening, as obtained from the InSAR inversion, nor the processes of vertical magma migration were simulated. However, our setup mirrors well the thickening of the dike after arrest. The evolution of the model was monitored with a digital top-view camera (resolution  $3456 \times 2304$  pixels), capturing one frame every 5 s, which is equivalent to one frame every 0.006 cm of dike opening. Digital images were then analyzed with MatPiv [Sveen, 2004], which is an open source software for particle image velocimetry running under the MATLAB package. This software uses a cross-correlation technique that allows calculating horizontal (in the x-y plane) displacement with about one tenth of a pixel of accuracy.

### 5.2. Analog Experiments of Volumetric Intrusion in Sand

We investigated how the surface displacement field and the fault pattern evolved from the top view photos of the analog model (Figure 6). During the initial stage of the opening (0.15 cm), no fault was visible in the rock analog (Figure 6a). We detected a subcircular patch with maximum displacement oriented orthogonally to the dike at about 0.01 cm (Figure 6e).

When the dike opening reached 0.3 cm, three distinct normal fault segments were apparent parallel to the direction of the dike (i.e., along the North axis) at the surface of the model (Figure 6b). The cumulative fault length was about 5 cm, and the location of the faults in the map view coincided with the shallowest part of the dike. The surface displacement pattern became clearer (Figure 6f), having a maximum displacement of about 0.1 cm about 7 cm from the dike.

When the opening of the dike increased to 0.45 cm, the fault pattern became more complex. Faults identified in the previous stage merged, reaching a cumulative length toward the North of about 10 cm. Two to three fault segments could be identified as moving outward from the dike plane. The fault strike remained mostly parallel to the dike axis, except for a minor outward deviation 2 cm toward the south (Figure 6c). Surface displacement also identified a subcircular patch with a maximum displacement of about 0.15 cm toward the east and a smaller region closer to the dike moving in the opposite direction (i.e., the north-south elongated light blue area close to the dike axis in Figure 6g); the latter confirms the activation of normal faults. At the final stage, when the dike opening reached 0.6 cm, fault traces clearly showed an inward convex shape in map view, which is consistent with the geometry of the dike. In fact, faults were more distant from the dike plane where the tip of the dike was deeper. The cumulative fault length was measured at about 12 cm (Figure 6d).

We also sampled cumulative displacement at 1, 5, and 10 cm from the dike plane, aligned along two sections (i.e., sections I and II) at 5 and 10 cm along the dike (Figures 6i and 6j). These two sections sampled two distinct portions of the dike, where it is 3.75 cm and 2.5 cm deep, respectively. Sampled points on the footwall of the normal faults appeared to be moving toward the east (Figure 6i). At first, the pace of eastward motion was slow (up to 0.2 cm of dike opening), but by the end of the experiment it reached a rather constant rate. The sampling point on the fault-hanging wall had approximately the opposite behavior. At the start, the displacement was stable up to 0.3 cm of dike opening, but it then started to move toward the west until the dike opening reached 0.4 cm, after which point it slowed down.

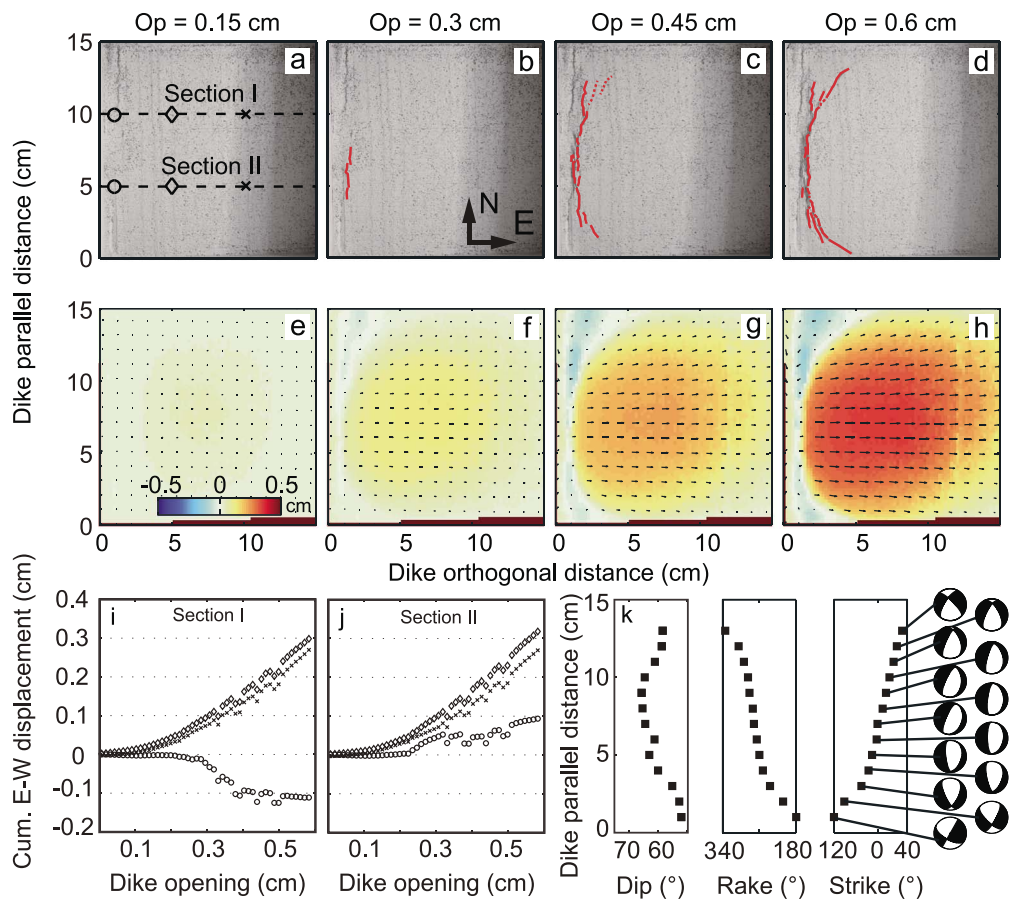


**Figure 6.** Experimental results showing the formation of faults caused by continuous dike opening. (a–d) Top-view photos of the surface of the model for increasing dike opening with the growing fault traced in red. (e–h) PIV analysis showing the magnitude of cumulative east-west displacements (background color) and the directions of displacement (arrows). (i, j) Cumulative eastward displacement of points located at 1 (circle), 5 (diamond), and 10 (cross) cm from the dike along sections I and II. (k) Fault dip, rake, and strike measured along the graben-bounding fault from south to north, along with predicted focal mechanisms.

We also measured the distance of the faults to the dike plane at every centimeter along the dike. Assuming that the faults join with the tip of the moving wall below [e.g., *Mastin and Pollard*, 1988] and because the dike depth at every point was known, we could calculate the average fault dip. Since the fault trace was not a simple line but distributed over some thickness, we report the average dip derived from the innermost and outermost faults. The average fault dip varies along the dike plane (i.e., toward the north, Figure 6k) with the central portion of the fault steeper (about 65–70°) than at the tips (55–60°). The cumulative surface displacement reached a maximum value of about 0.4 cm at a distance of about 7 cm from the dike plane. The rake of the fault motion rotates progressively along the fault from oblique left lateral to dip slip to oblique right lateral moving from north to south along the main surface fault (Figure 6k).

## 6. Discussion

Our time series of InSAR measurements allows us to roughly estimate the duration and speed of the magma ascent. The InSAR observations show no significant ground deformation up to 8 May (not shown here) and then strong ground deformation associated with the ~2 km deep dike on 16 May, which is the next available Envisat image of the area. According to this information, we can estimate the minimum depth of the dike on 8 May such that it was undetectable by InSAR, assuming that the volume of the dike remained the same during its upward propagation (i.e., incompressible magma and negligible additional inflow from below). If we take the InSAR detection threshold to be 5 mm and assume that the dike was vertical and had a volume of  $0.06 \text{ km}^3$ , then the dike was deeper than 20 km below the surface on 8 May. This suggests that the source

of the magma was deep and possibly below the Moho, which has been estimated at ~35 km depth below Harrat Lunayyir [Hansen *et al.*, 2007]. This also indicates that the dike propagated upward at a velocity faster than ~2 km/d between 8 and 16 May.

From 16 to 19 May, the dike slowed down and ascended by only about 1 km, causing the extensive surface fissuring and faulting. The propagation velocity during the first stage is of the same order as has been found for other dikes ascending the last few kilometers of the crust before erupting. Prior to the March 1998 Piton de la Fournaise eruption, the migration velocity of the dike decreased from 2.28 km/d between 5 km and 1.5 km below sea level to 1.8 km/d between 1.5 km below sea level and the surface [Battaglia *et al.*, 2005]. The lateral intrusions during the Dabbahu rifting episode propagated at higher velocities of 15–65 km/d and also several intrusions of the Krafla rifting episode at 35–100 km/d [Buck *et al.*, 2006]. The approximate exponential deceleration of the Krafla and Afar dikes has been attributed to loss of pressurization due to decompression at the magma reservoir [Buck *et al.*, 2006; Rivalta, 2010]. The lower velocity of the Harrat Lunayyir dike suggests low buoyancy and an efficient decoupling from a pressurized feeding reservoir, which is consistent with a deep source of the magma and the lack of a broad subsidence signal that could be attributed to reservoir deflation.

Our results suggest that the dike decelerated significantly during the final stages of the emplacement at Harrat Lunayyir. In addition to pressure loss at a feeding magma chamber as mentioned above, which is likely not relevant for the Harrat Lunayyir dike, many factors may accelerate or decelerate a dike during its path toward the free surface [Rivalta *et al.*, 2015]: solidification [Taisne *et al.*, 2011a], layering [Rivalta and Dahm, 2004; Taisne *et al.*, 2011b], and topographic loads [Watanabe *et al.*, 2002; Maccaferri *et al.*, 2011]. When a dike is close to the free surface, it is predicted to accelerate, as observations [Battaglia *et al.*, 2005], laboratory experiments [Rivalta and Dahm, 2006], and theoretical studies [Pollard and Holzhausen, 1979] have shown. Often, the increase of magma pressure and ascending velocity leads to eruptions. However, analog experiments have shown that slip on preexisting fractures tends to decelerate dike velocity [Le Corvec *et al.*, 2013]. In the case of the Harrat Lunayyir dike, the dominant factor causing the dike to decelerate and eventually stop was probably the interaction with the graben faulting. The Harrat Lunayyir dike event therefore bears some similarities with the 2007 Natron intrusion in Tanzania, where strong dike-fault interactions were also observed [Calais *et al.*, 2008]. A loss of buoyancy due to a decreased density difference between host rock and magma may also have contributed to decelerating the dike, but the fact that the dike continued to inflate after its arrest demonstrates that the magma was still buoyant at the depth of the dike arrest. It is also possible that the dike became arrested at the depth expected from the overall density profile of the crust and magma and that the continuous bulging of the arrested dike due to inflow of magma from the dike tail was responsible for the intense stressing leading to the graben faults. Based on a numerical model Maccaferri *et al.* [2016] suggested that seismic and aseismic slip on preexisting faults arrested the 2000 Miyakejima dike intrusion and that further inflation of the arrested dike caused additional seismic and aseismic faulting. Our observations and stress calculations indicate that the graben-bounding faulting due to the shallow Harrat Lunayyir dike intrusion played an important role in stalling the dike ascent and preventing an eruption. The dike was arrested in the shallow crust, but it kept inflating as buoyant magma continued to flow from below; the increasing opening of the dike caused further movements on the graben-bounding normal faults, producing small-magnitude earthquakes for a period of time, as seen in Figure 2b. The persistent small-magnitude seismicity might suggest that pressure continued to evolve after the intrusion or that slow-slip movements of the graben-bounding faults continued throughout the sequence [Bean *et al.*, 2014].

The analog experiment has high resolution in both space and time, and therefore, it provides additional insights on the fracture initiation, fault growth, and graben evolution. The arched shape of the dike's top edge at shallow depths leads to similarly arch-shaped graben faults at the surface. In particular, the narrowest part of the graben is observed directly above the shallowest part of the dike. Similar observations were reported for the recent Bárðarbunga dike intrusion (J. Ruch *et al.*, in revision, 2016), where graben-bounding normal faults converge toward the location where the dike erupted, and at Medicine Lake Volcano, where a wider graben is found and where a dike intrusion propagated under a hill [Fink and Pollard, 1983]. The graben-bounding faults first initiate near the shallowest part of the dike and then propagate outward in response to increasing dike opening. The propagation occurs by successive formation of small fractures that start with variable orientation and then later merge into a well-developed graben fault. The deeper the dike is the more intense stresses are needed to reach the failure threshold, and the surface stress concentrations leading to faulting are located farther away from the dike plane [Tripanera *et al.*, 2015]. In our experiment, the rake rotates progressively from pure dip slip at the center of the graben to increasingly more strike slip toward the ends of the graben-

bounding faults (Figure 6k). Such a mix of variable focal mechanisms has commonly been observed during dike intrusions; for example, *Passarelli et al.* [2015] found that most normal faulting events occurred above the intruding dike during the 2000 intrusion at Miyakejima, while strike-slip faulting occurred near the tips of the dike, with oblique mechanisms observed in between.

Our results highlight differences between dike-induced faulting and tectonic faulting. Tectonic faulting mainly occurs on major fault planes and has largely homogeneous focal mechanisms. Strain accumulates on the main fault interseismically and is then released when an earthquake occurs. Dike-induced faults, on the other hand, tend to form where the dilatational strain is highest at shallow depths on either side (or both) of an intruding dike, producing normal faulting earthquakes that gradually contain more strike slip toward the ends of the graben-bounding faults (Figure 6k). While dike intrusions cause earthquake swarms, most of the energy of graben-bounding faulting is released aseismically [*Ozawa et al.*, 2004; *Pallister et al.*, 2010]. Our study of the temporal evolution of the Harrat Lunayyir dike and faults, taken together with our analog experiment suggests that the observations are consistent with a slowly varying and spatially inhomogeneous (both in terms of intensity and orientation of principal stresses) dike-induced stressing rate [*Passarelli et al.*, 2015]. Such time-dependent forcing makes dike-induced faulting dynamically different from tectonic faulting but possibly similar to faulting induced by slow fluid-driven processes. In our analog experiment we show how the slow, inhomogeneous dike-induced stressing interacts with the weak rheology of a granular material (analog to the topmost crustal layers) in generating a faulting process consistent with observations of the Harrat Lunayyir activity and other dike events around the world.

## 7. Conclusions

The combination of InSAR observations, stress calculations, and analog experiments enabled us to analyze the interplay between the dike intrusion and normal faulting during the 2009 Harrat Lunayyir magma-driven earthquake swarm. Although the InSAR data were acquired in different imaging modes, in different orbits, and with different incidence angles, they provide detailed spatial and temporal evolution of the ground deformation. Modeling of the InSAR observations shows that the rifting event initiated with a dike injection propagating to a shallow depth that subsequently induced graben-bounding normal faulting.

The  $\Delta CFS$  calculations show that a shallow dike intrusion increases compression adjacent to the dike and induces extension above it, leading to formation of graben-bounding normal faults. Results from the analog experiment indicate that the graben-bounding faults first form near the shallowest part of the dike and then propagate outward to form a wedge-shaped graben. Slip on the graben-bounding normal faults acts in return against further vertical propagation of the dike by stress clamping, causing its arrest at shallow depths.

The Harrat Lunayyir intrusion was the first intrusive event to occur on the eastern flank of the Red Sea rift in a modern space geodetic era. This event suggests that the off-rift volcanoes remain active and potentially hazardous. Rapid urbanization and population growth in the western part of Saudi Arabia has led to increased volcanic risk in the area. More knowledge of the regional volcanic activity and magma plumbing systems should thus help in assessing the volcanic hazard in the region. As the seismic networks on the Arabian Peninsula expand, more volcano tectonic earthquakes will be detected. In addition, new InSAR satellite missions (e.g., Sentinel-1 and ALOS-2) will offer more frequent imaging of the region and provide better data of volcanic deformation.

### Acknowledgments

We thank Samantha Hansen (University of Alabama) for earthquake locations and Luigi Passarelli (GFZ) for useful discussions. We thank the Associate Editor Mike Poland and two anonymous reviewers for helpful comments. The SAR images were provided by the European Space Agency (ESA) through the Category-1 project 6703. The GMT software [Wessel and Smith 1998] was used to prepare Figure 1. The research reported in this publication was supported by King Abdullah University of Science and Technology (KAUST). E.R. and F.C. were funded by the European Union through the ERC StG Project CCMP-POMPEI, grant 240583.

## References

- ArRajehi, A., et al. (2010), Geodetic constraints on present-day motion of the Arabian Plate: Implications for Red Sea and Gulf of Aden rifting, *Tectonics*, 29, TC3011, doi:10.1029/2009TC002482.
- Baer, G., and Y. Hamiel (2010), Form and growth of an embryonic continental rift: InSAR observations and modelling of the 2009 western Arabia rifting episode, *Geophys. J. Int.*, 182, 155–167.
- Baer, G., Y. Hamiel, G. Shamir, and R. Nof (2008), Evolution of a magma-driven earthquake swarm and triggering of the nearby Oldoinyo Lengai eruption, as resolved by InSAR, ground observations and elastic modeling, East African Rift, 2007, *Earth Planet. Sci. Lett.*, 272, 339–352.
- Bardsley, J. M., A. Solonen, H. Haario, and M. Laine (2014), Randomize-then-optimize: A method for sampling from posterior distributions in nonlinear inverse problems, *Siam J. Sci. Comput.*, 36, A1895–A1910.
- Battaglia, J., V. Ferrazzini, T. Staudacher, K. Aki, and J. L. Cheminée (2005), Pre-eruptive migration of earthquakes at the Piton de la Fournaise volcano (Réunion Island), *Geophys. J. Int.*, 161, 549–558.
- Bean, C. J., L. De Barros, I. Lokmer, J.-P. Metaxian, G. O’ Brien, and S. Murphy (2014), Long-period seismicity in the shallow volcanic edifice formed from slow-rupture earthquakes, *Nat. Geosci.*, 7, 71–75.

- Biggs, J., F. Amelung, N. Gourmelen, T. H. Dixon, and S. W. Kim (2009), InSAR observations of 2007 Tanzania rifting episode reveal mixed fault and dyke extension in an immature continental rift, *Geophys. J. Int.*, 179, 549–558.
- Biggs, J., M. Chivers, and M. C. Hutchinson (2013), Surface deformation and stress interactions during the 2007–2010 sequence of earthquake, dyke intrusion and eruption in northern Tanzania, *Geophys. J. Int.*, 195, 16–26.
- Buck, W. R., P. Einarsson, and B. Brandsdóttir (2006), Tectonic stress and magma chamber size as controls on dike propagation: Constraints from the 1975–1984 Krafla rifting episode, *J. Geophys. Res.*, 111, B12404, doi:10.1029/2005JB003879.
- Calais, E., et al. (2008), Strain accommodation by slow slip and dyking in a youthful continental rift, East Africa, *Nature*, 456, 783–787.
- Camp, V. E., P. R. Hooper, M. J. Roobol, and D. L. White (1987), The Madinah eruption, Saudi Arabia: Magma mixing and simultaneous extrusion of three basaltic chemical types, *Bull. Volcanol.*, 49, 489–508.
- Cervelli, P., M. H. Murray, P. Segall, Y. Aoki, and T. Kato (2001), Estimating source parameters from deformation data, with an application to the March 1997 earthquake swarm off the Izu Peninsula, Japan, *J. Geophys. Res.*, 106(B6), 11,217–11,237, doi:10.1029/2000JB900399.
- Chen, C. W., and H. A. Zebker (2000), Network approaches to two-dimensional phase unwrapping: Intractability and two new algorithms, *J. Opt. Soc. Am.*, 17, 401–414.
- Duncan, R. A., and A. M. Al-Amri (2013), Timing and composition of volcanic activity at Harrat Lunayyir, western Saudi Arabia, *J. Volcanol. Geotherm. Res.*, 260, 103–116.
- Ebinger, C., A. Ayele, D. Keir, J. Rowland, G. Yirgu, T. Wright, M. Belachew, and I. Hamling (2010), Length and timescales of rift faulting and magma intrusion: The Afar rifting cycle from 2005 to present, *Annu. Rev. Earth Planet. Sci.*, 38, 439–466.
- Farr, T. G., et al. (2007), The shuttle radar topography mission, *Rev. Geophys.*, 45, RG2004, doi:10.1029/2005RG000183.
- Fink, J. H., and D. D. Pollard (1983), Structural evidence for dikes beneath silicic domes, Medicine Lake Highland Volcano, California, *Geology*, 11, 458–461, doi:10.1130/0091-7613.
- Freed, A. M. (2005), Earthquake triggering by static, dynamic, and postseismic stress transfer, *Annu. Rev. Earth Planet. Sci.*, 33, 335–367.
- Goldstein, R. M., and C. L. Werner (1998), Radar interferogram filtering for geophysical applications, *Geophys. Res. Lett.*, 25, 4035–4038, doi:10.1029/1998GL900033.
- Grandin, R., et al. (2009), September 2005 Manda Hararo-Dabbahu rifting event, Afar (Ethiopia): Constraints provided by geodetic data, *J. Geophys. Res.*, 114, B08404, doi:10.1029/2008JB005843.
- Grandin, R., A. Socquet, E. Jacques, N. Mazzoni, J. B. de Chabalier, and G. C. P. King (2010), Sequence of rifting in Afar, Manda-Hararo rift, Ethiopia, 2005–2009: Time-space evolution and interactions between dikes from interferometric synthetic aperture radar and static stress change modeling, *J. Geophys. Res.*, 115, B10413, doi:10.1029/2009JB000815.
- Hamling, I. J., A. Ayele, L. Bennati, E. Calais, C. J. Ebinger, D. Keir, E. Lewi, T. J. Wright, and G. Yirgu (2009), Geodetic observations of the ongoing Dabbahu rifting episode: New dyke intrusions in 2006 and 2007, *Geophys. J. Int.*, 178, 989–1003.
- Hamling, I. J., T. J. Wright, E. Calais, L. Bennati, and E. Lewi (2010), Stress transfer between thirteen successive dyke intrusions in Ethiopia, *Nat. Geosci.*, 3, 713–717.
- Hansen, S. E., A. J. Rodgers, S. Y. Schwartz, and A. M. Al-Amri (2007), Imaging ruptured lithosphere beneath the Red Sea and Arabian Peninsula, *Earth Planet. Sci. Lett.*, 259, 256–265.
- Hansen, S. E., H. R. DeShon, M. M. Moore-Driskell, and A. M. S. Al-Amri (2013), Investigating the *P* wave velocity structure beneath Harrat Lunayyir, northwestern Saudi Arabia, using double-difference tomography and earthquakes from the 2009 seismic swarm, *J. Geophys. Res. Solid Earth*, 118, 4814–4826, doi:10.1002/jgrb.50286.
- Hubbert, M. K. (1937), Theory of scale models as applied to the study of geologic structures, *Geol. Soc. Am. Bull.*, 48, 1459–1520.
- Jónsson, S. (2012), Tensile rock mass strength estimated using InSAR, *Geophys. Res. Lett.*, 39, L21305, doi:10.1029/2012GL053309.
- Jónsson, S., H. Zebker, P. Segall, and F. Amelung (2002), Fault slip distribution of the 1999 *Mw* 7.1 Hector Mine, California, earthquake, estimated from satellite radar and GPS measurements, *Bull. Seismol. Soc. Am.*, 92, 1377–1389.
- Koulakov, I., S. El Khrepy, N. Al-Arif, I. Sychev, and P. Kuznetsov (2014), Evidence of magma activation beneath the Harrat Lunayyir basaltic field (Saudi Arabia) from attenuation tomography, *Solid Earth*, 5, 873–882.
- Koulakov, I., S. El Khrepy, N. Al-Arif, P. Kuznetsov, and E. Kasatkina (2015), Structural cause of a missed eruption in the Harrat Lunayyir basaltic field (Saudi Arabia) in 2009, *Geology*, 43, 395–398, doi:10.1130/G36271.1.
- Le Corvec, N., T. Menand, and J. Lindsay (2013), Interaction of ascending magma with pre-existing crustal fractures in monogenetic basaltic volcanism: An experimental approach, *J. Geophys. Res. Solid Earth*, 118, 968–984, doi:10.1002/jgrb.50142.
- Lin, J., and R. S. Stein (2004), Stress triggering in thrust and subduction earthquakes and stress interaction between the southern San Andreas and nearby thrust and strike-slip faults, *J. Geophys. Res.*, 109, B02303, doi:10.1029/2003JB002607.
- Maccaferri, F., M. Bonafede, and E. Rivalta (2011), A quantitative study of the mechanisms governing dike propagation, dike arrest and sill formation, *J. Volcanol. Geotherm. Res.*, 208, 39–50.
- Maccaferri, F., E. Rivalta, L. Passarelli, and Y. Aoki (2016), On the mechanisms governing dike arrest: Insight from the 2000 Miyakejima dike injection, *Earth Planet. Sci. Lett.*, 434, 64–74.
- Mastin, L. G., and D. D. Pollard (1988), Surface deformation and shallow dike intrusion processes at Inyo Craters, Long Valley, California, *J. Geophys. Res.*, 93, 13,221–13,235, doi:10.1029/JB093B11p13221.
- Nobile, A., C. Pagli, D. Keir, T. J. Wright, A. Ayele, J. Ruch, and V. Acocella (2012), Dike-fault interaction during the 2004 Dallol intrusion at the northern edge of the Erta Ale Ridge (Afar, Ethiopia), *Geophys. Res. Lett.*, 39, L19305, doi:10.1029/2012GL053152.
- Norini, G., and V. Acocella (2011), Analogue modeling of flank instability at Mount Etna: Understanding the driving factors, *J. Geophys. Res.*, 116, B07206, doi:10.1029/2011JB008216.
- Okada, Y. (1985), Surface deformation due to shear and tensile faults in a half-space, *Bull. Seismol. Soc. Am.*, 75, 1135–1154.
- Ozawa, S., S. Miyazaki, T. Nishimura, M. Murakami, M. Kaidzu, T. Imakiire, and X. Ji (2004), Creep, dike intrusion, and magma chamber deflation model for the 2000 Miyake eruption and the Izu islands earthquakes, *J. Geophys. Res.*, 109, B02410, doi:10.1029/2003JB002601.
- Pallister, J. S., et al. (2010), Broad accommodation of rift-related extension recorded by dike intrusion in Saudi Arabia, *Nat. Geosci.*, 3, 705–712.
- Passarelli, L., F. Maccaferri, E. Rivalta, T. Dahm, and E. Abebe Boku (2012), A probabilistic approach for the classification of earthquakes as “triggered” or “not triggered”, *J. Seismol.*, 17, 165–187.
- Passarelli, L., E. Rivalta, S. Cesca, and Y. Aoki (2015), Stress changes, focal mechanisms, and earthquake scaling laws for the 2000 dike at Miyakejima (Japan), *J. Geophys. Res. Solid Earth*, 120, 4130–4145, doi:10.1002/2014JB011504.
- Pollard, D. D., and G. Holzhausen (1979), On the mechanical interaction between a fluid-filled fracture and the earth's surface, *Tectonophysics*, 53, 27–57.
- Rivalta, E. (2010), Evidence that coupling to magma chambers controls the volume history and velocity of laterally propagating intrusions, *J. Geophys. Res.*, 115, B07203, doi:10.1029/2009JB006922.

- Rivalta, E., and T. Dahm (2004), Dyke emplacement in fractured media: Application to the 2000 intrusion at Izu islands, Japan, *Geophys. J. Int.*, 157, 283–292.
- Rivalta, E., and T. Dahm (2006), Acceleration of buoyancy-driven fractures and magmatic dikes beneath the free surface, *Geophys. J. Int.*, 166, 1424–1439.
- Rivalta, E., B. Taisne, A. P. Bunger, and R. F. Katz (2015), A review of mechanical models of dike propagation: Schools of thought, results and future directions, *Tectonophysics*, 638, 1–42.
- Roobol, M. J. (2009), Geology, structure and seismicity of Harrat Lunayyir volcanic field. Al-Eis region, northwestern Saudi Arabia, *Saudi Geol. Surv. Rep.* 14.
- Rowland, J. V., E. Baker, C. J. Ebinger, D. Keir, T. Kidane, J. Biggs, N. Hayward, and T. J. Wright (2007), Fault growth at a nascent slow-spreading ridge: 2005 Dabbahu rifting episode, Afar, *Geophys. J. Int.*, 171, 1226–1246.
- Rubin, A. M., and D. D. Pollard (1988), Dike-induced faulting in rift zones of Iceland and Afar, *Geology*, 16, 413–417.
- Ruch, J., V. Acocella, N. Geshi, A. Nobile, and F. Corbi (2012), Kinematic analysis of vertical collapse on volcanoes using experimental models time series, *J. Geophys. Res.*, 117, B07301, doi:10.1029/2012JB009229.
- Sveen, J. K. (2004), An introduction to MatPIV v.1.6.1, in *Mechanics and Applied Mathematics*, 27 pp., Dept. of Math., Univ. of Oslo, Oslo.
- Sigmundsson, F., et al. (2015), Segmented lateral dyke growth in a rifting event at Bárðarbunga volcanic system, Iceland, *Nature*, 517, 191–195.
- Taisne, B., F. Brenguier, N. M. Shapiro, and V. Ferrazzini (2011a), Imaging the dynamics of magma propagation using radiated seismic intensity, *Geophys. Res. Lett.*, 38, L04304, doi:10.1029/2010GL046068.
- Taisne, B., S. Tait, and C. Jaupart (2011b), Conditions for the arrest of a vertical propagating dyke, *Bull. Volcanol.*, 73, 191–204.
- Toda, S., R. S. Stein, K. Richards-Dinger, and S. B. Bozkurt (2005), Forecasting the evolution of seismicity in southern California: Animations built on earthquake stress transfer, *J. Geophys. Res.*, 110, B05S16, doi:10.1029/2004JB003415.
- Tripannera, D., V. Acocella, and J. Ruch (2014), Dike-induced contraction along oceanic and continental divergent plate boundaries, *Geophys. Res. Lett.*, 41, 7098–7104, doi:10.1002/2014GL061570.
- Tripannera, D., J. Ruch, V. Acocella, and E. Rivalta (2015), Experiments of dike-induced deformation: Insights on the long-term evolution of divergent plate boundaries, *J. Geophys. Res. Solid Earth*, 120, 6913–6942, doi:10.1002/2014JB011850.
- Watanabe, T., T. Masuyama, K. Nagaoka, and T. Tahara (2002), Analog experiments on magma-filled cracks: Competition between external stresses and internal pressure, *Earth Planets Space*, 54, 1247–1262.
- Wessel, P., and W. H. F. Smith (1998), New, improved version of generic mapping tools released, *Eos Trans. AGU*, 79(47), 579–579, doi:10.1029/98EO00426.
- Wright, T. J., C. Ebinger, J. Biggs, A. Ayele, G. Yirgu, D. Keir, and A. Stork (2006), Magma-maintained rift segmentation at continental rupture in the 2005 Afar dyking episode, *Nature*, 442, 291–294.
- Wright, T. J., et al. (2012), Geophysical constraints on the dynamics of spreading centres from rifting episodes on land, *Nat. Geosci.*, 5, 242–250.